Jupiter Evolutionary Models Incorporating Stably Stratified Regions

Roberto Tejada Arevalo [ID],[1] Ankan Sur [ID],[1] Yubo Su [ID],[1] and Adam Burrows [ID][1, 2]

[1]*Department of Astrophysical Sciences, Princeton University, 4 Ivy Lane, Princeton, NJ 08544, USA*
[2]*Institute for Advanced Study, 1 Einstein Dr, Princeton, NJ 08540, USA*

ABSTRACT

We address the issue of which broad set of initial conditions for the planet Jupiter best matches the current presence of a "fuzzy core" of heavy elements, while at the same time comporting with measured parameters such as its effective temperature, atmospheric helium abundance, radius, and atmospheric metallicity. Our focus is on the class of fuzzy cores that can survive convective mixing to the present day and on the unique challenges of an inhomogeneous Jupiter with stably-stratified regions now demanded by the *Juno* gravity data. Hence, using the new code `APPLE`, we attempt to put a non-adiabatic Jupiter into an evolutionary context. This requires not only a mass density model, the major relevant byproduct of the *Juno* data, but a thermal model that is subject to interior heat transport, a realistic atmospheric flux boundary, a helium rain algorithm, and the latest equation of state. The result is a good fit to most major thermal, compositional, and structural constraints that still preserve a fuzzy core and that should inform future more detailed models of the current Jupiter in the context of its evolution from birth.

Keywords: Solar system gas giant planets, Extrasolar gaseous giant planets, Planetary science, Planetary structure

1. INTRODUCTION

The *Juno* (Bolton et al. 2017) and *Cassini* (Matson et al. 2003) missions have significantly transformed our knowledge of the current interiors of Jupiter and Saturn, revealing the presence of high heavy element enrichment at depth and the possible presence of convectively stable regions and extended heavy-element cores (Fuller et al. 2014; Fuller 2014; Wahl et al. 2017; Folkner et al. 2017; Nettelmann 2017; Iess et al. 2019; Militzer et al. 2019; Debras & Chabrier 2019; Durante et al. 2020; Mankovich & Fuller 2021; Nettelmann et al. 2021; Militzer et al. 2022; Militzer & Hubbard 2024). In addition, over the past decade exoplanet research is starting to reveal the masses, sizes, and demographic characteristics of thousands of exoplanets (e.g., see Winn & Fabrycky 2015; Fulton et al. 2017; Petigura et al. 2018; Rosenthal et al. 2021). Furthermore, missions such as *JWST* (Gardner et al. 2006) and future ventures, including *PLATO* (Rauer et al. 2014), and *ARIEL* (Tinetti et al. 2021),

are poised to launch a new era of exoplanet exploration. This ferment suggests that it is timely to attempt a deeper understanding of the structure and evolution of Solar System gas giant planets, in part to advance our knowledge of gas giant exoplanet formation and evolution.

Recent discoveries of extended heavy element (Z) regions within Jupiter and Saturn may offer insight into their formation and evolution. The top panel of Figure 1 illustrates four examples of initial composition profiles from formation models of Jupiter, as presented by Vazan et al. (2016), Lozovsky et al. (2017), Helled & Stevenson (2017), and Stevenson et al. (2022). The bottom panel displays the current inferred heavy-element distribution of Jupiter, as derived from *Juno* gravity data by Militzer & Hubbard (2024), Militzer et al. (2022), Nettelmann et al. (2021), Debras & Chabrier (2019), and Wahl et al. (2017). These present-day heavy-element distributions of Jupiter encompass a wide range of possibilities that agree with the *Juno* data, though only a limited number of evolutionary models have incorporated formation-based initial conditions (Müller et al. 2020; Stevenson et al. 2022). Evolutionary models informed by formation models have faced challenges in re-

Corresponding author: Roberto Tejada Arevalo
arevalo@princeton.edu

producing the heavy-element profiles observed by *Juno* (Müller et al. 2020). More recently, Stevenson et al. (2022) provided formation models that preserve until the current epoch a dilute core with an extent between 0.33 R_J and 0.44 R_J, in rough agreement with the formation models of Müller et al. (2020) and Lozovsky et al. (2017). Particularly, the initial thermal profiles from formation models frequently lead to homogeneous composition profiles. The initial high interior entropies in the formation profiles used by Müller et al. (2020) led to extensive convective mixing throughout much of the extended core region over Gyr timescales.

Thus far, evolutionary studies incorporating Jovian extended cores have left open the questions of 1) which broad set of initial conditions are best suited to match the current presence of a fuzzy core and measured parameters and 2) the character of helium phase separation expected to occur in Jupiter (Stevenson 1975; Wilson & Militzer 2010; Hubbard & Militzer 2016; Mankovich et al. 2016; Mankovich & Fortney 2020; Nettelmann et al. 2024; Howard et al. 2024). We note that past work involving evolutionary models with fuzzy cores (e.g., Vazan et al. 2018; Stevenson et al. 2022) did not account for the evolutionary effects of helium rain on Jupiter's atmospheric helium abundance. To begin to address the question of the possible preservation of a fuzzy core from birth, Knierim & Helled (2024) showed that cooler interior entropy (S) profiles might maintain an extended initial Z profile over evolutionary timescales. In contrast, hotter interior S profiles lead to convective mixing and homogenization over shorter timescales due to the expansion of the outer convective zone. Those authors concluded that the primordial entropy profile is the dominant factor shaping the evolution of the composition profile and broader planetary structure. Their conclusions inform formation models and evolutionary calculations, but leave open the question of how Jupiter's current effective temperature and atmospheric helium mass fraction can be explained.

In this paper, we address these two aspects simultaneously. We conduct evolutionary models to determine general initial distributions of heavy elements that can best match Jupiter's current effective temperature ($T_{\text{eff}} = 125.57$ K; Li et al. 2012), the atmospheric helium abundance as measured by the *Galileo* entry probe ($Y_{\text{atm}} = 0.234 \pm 0.005$; Von Zahn et al. 1998), the outer metallicity abundance of roughly three solar ($\sim 3Z_{\odot}$) as measured by *Voyager*, *Galileo*, and *Juno* (see Helled & Howard 2024; Guillot et al. 2022; Li et al. 2020), and the current equatorial radius of Jupiter (71,492 km; Seidelmann et al. 2007), while still preserving an extended heavy-element core. These values are sum-

marized in Table 1. This work presents the first evolutionary models of Jupiter with extended cores with helium rain, updated atmospheric boundary conditions that account for ammonia clouds, irradiation, and helium abundance dependence (Chen et al. 2023), the most current hydrogen-helium (H-He) and Z equations of state (EOS) (Chabrier & Debras 2021; Haldemann et al. 2020), and the best available pressure, temperature, and Y-dependent H-He miscibility curves (Lorenzen et al. 2009, 2011; Schöttler & Redmer 2018).

In §2, we describe our evolutionary code, **APPLE** (Sur et al. 2024), our updated boundary conditions (Chen et al. 2023), the EOSes used for the envelope and compact core, and the H-He miscibility curves used for all models (Tejada Arevalo et al. 2024). Throughout this work, we use the term "compact core" to refer to the inner rocky, "$Z = 1$" region and use "fuzzy," "extended," or "dilute," core interchangeably to indicate the region of the envelope with enhanced Z and/or where $dZ/dm < 0$, where m is the interior mass. In §3, we provide a set of models with varying initial conditions. We vary the total entropy profile and the sizes of the extended cores and determine which initial conditions best preserve a fuzzy core, while approximately matching Jupiter's current effective temperature and radius. Section §4 presents one favored Jupiter model that closely matches the observables in Table 1 and describes the parameters necessary to obtain this model. We provide concluding remarks in §5.

Table 1. Present-day Jupiter Observables Considered

Parameter	Value
T_{eff} [Kelvin]	125.57 ± 0.07
Y_{atm}	0.234 ± 0.005
$Z_{\odot}$ (out)	1.5–5 ($\sim$3)
Equatorial Radius [km]	$71,492 \pm 4$

NOTE—The effective temperature comes from Li et al. (2012), the atmospheric helium abundance from Von Zahn et al. (1998), the outer metallicity from various measurements of the atmosphere (Li et al. 2020), and the radius measurements come from Seidelmann et al. (2007). The metal abundances can range between 1.5 and 5 solar but have a concentration of roughly 3 times solar (Figure 2 of Helled & Howard 2024)
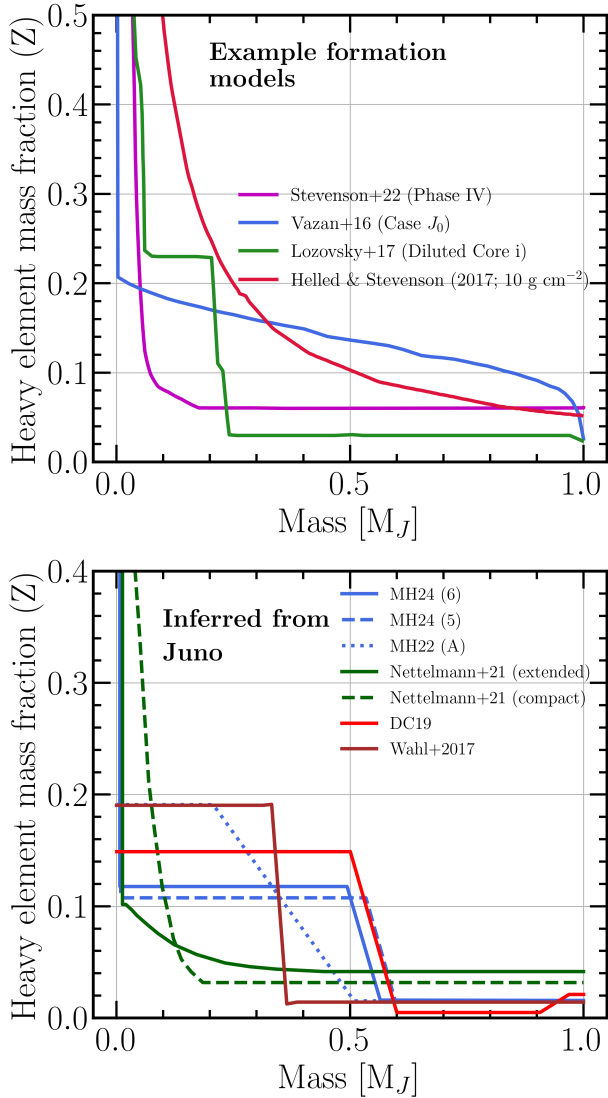
Figure 1. Top: Examples of the distribution of Z for formation models from Stevenson et al. (2022), Vazan et al. (2016), Lozovsky et al. (2017), and Helled & Stevenson (2017). The profile names are also given since these authors explored multiple models. These formation distributions are taken at the time when the proto-Jupiters reached final mass according to the authors. Bottom: Current composition gradients as inferred by the *Juno* gravity data from Militzer & Hubbard (2024, MH24), Militzer et al. (2022, MH22), Nettelmann et al. (2021), Debras & Chabrier (2019, DC19), and Wahl et al. (2017), as adapted by Helled et al. (2022). The heavy element distributions inferred by various authors using the *Juno* data employ different methods, equations of state, and assumptions concerning the current thermal profile of Jupiter. These differences can potentially account for the differences seen in the inferred Z profiles. Hence, even though *Juno* provided precise values of the J_{2n} gravity moments, there remains a large range of potential Z distributions that might explain the *Juno* data.

2. METHODS

The evolutionary models presented throughout are calculated using `APPLE` (Sur et al. 2024) and include the effects of solid-body rotation via conservation of angular momentum (see Equation 1 of Sur et al. 2024). A final spin period of 9:55:29.704 hr is assumed (Yu & Russell 2009) and we neglect differential rotation. All models calculate and compare to the equatorial radius of Jupiter. Moreover, all models include the precomputed and irradiated atmospheric boundary condition tables of of Chen et al. (2023). These boundary conditions are improvements upon the Fortney et al. (2011) boundary conditions in that they include solar insolation in the detailed atmosphere calculation, the effects of ammonia clouds, and naturally obtain the updated albedo of Jupiter of 0.5 (Li et al. 2018). We use the H-He EOS of Chabrier & Debras (2021, CD21) and mix it via the volume addition law (see Tejada Arevalo et al. 2024; Chabrier et al. 2019; Saumon et al. 1995, for details) with the latest multi-phase water EOS tables from Haldemann et al. (2020, AQUA), which includes the supercritical and superionic water EOS of Mazevet et al. (2019).

The most recent theoretical H-He miscibility work is that of Schöttler & Redmer (2018, herein SR18). Both SR18 and the older (and hotter) miscibility curves of Lorenzen et al. (2009, 2011, herein LHR0911) are thus far the most flexible Y-dependent ab initio H-He miscibility curves publicly available. We use both of these miscibility curves in this work and adjust, as has been done in past evolutionary work (Nettelmann et al. 2015; Püstow et al. 2016; Mankovich et al. 2016; Mankovich & Fortney 2020; Howard et al. 2024), the temperatures of their miscibility curves at a given pressure and Y fraction when trying to obtain the current helium abundance of Jupiter's atmosphere. We note that recent experimental work on H-He phase separation (Brygoo et al. 2021) disagrees with the theoretical demixing temperatures result of LHR0911 and SR18 (see Tejada Arevalo et al. 2024, for a detailed discussion). The experimental H-He demixing results of Brygoo et al. (2021) find higher immiscibility temperatures by as much as 7,000 K and 3,000 K compared to the theoretical work of SR18 and LHR0911, respectively.

In the absence of any detailed knowledge of helium droplet formation (Stevenson & Salpeter 1977; Mankovich et al. 2016) in regions of expected H-He phase separation ($\sim$1–3 Mbar), `APPLE` uses advection-diffusion methods to transport helium in the miscibility region toward the inner convective regions (see equation 49 in Sur et al. 2024), while conserving total helium mass to machine precision. In all our evolution-

ary calculations, we identify the corresponding helium mass fraction at immiscibility ($Y_{\mathrm{misc}}(P, T)$) at the local temperatures and pressures of each Jupiter profile. To determine an immiscible region, we compare the adjusted helium mass fraction ($Y' = Y/(Y + X)$, where X is the hydrogen mass fraction) with $Y_{\mathrm{misc}}(P, T)$. If $Y_{\mathrm{misc}}(P, T) < Y'$, then APPLE deploys a modified advection term in the diffusion equation to model helium rain (see section 5.4.2 of Sur et al. 2024).

The regions unstable to convection are determined via the Ledoux criterion,

$$\frac{\partial S}{\partial r} - \sum_i \left(\frac{\partial S}{\partial X_i}\right)_{\rho, P} \frac{\partial X_i}{\partial r} < 0\,, \qquad (1)$$

where the X_i are the helium (Y) and heavy-element (Z) mass fractions. A full derivation of this criterion can be found in Tejada Arevalo et al. (2024). The EOS tables and a full description of these derivatives are also found in Tejada Arevalo et al. (2024).

In convective regions, a mixing-length flux procedure for both energy and composition, as described in Sur et al. (2024), is employed. Equation 1 is tested at every mass zone and if the convective condition is satisfied, we add the convective flux to the conductive heat flux. However, as discussed in Gabriel et al. (2014), determining the stable-convective boundary is not a trivial problem and the determination and effects of the stable-convective boundary have been the subject of intense study in stellar evolution circles. Our application of the Ledoux condition assumes that the convective boundary zone is located between the last convective zone and the first stable zone, introducing a discontinuity in the Ledoux condition derivatives. The challenges in determining the stable-convective boundary regions are many and there is currently no best practice adopted by the stellar or planetary evolutionary community. This is an important challenge that the stellar and planetary evolution communities should resolve in the near future.

In stably-stratified regions, the conductive thermal and compositional fluxes are calculated using the French et al. (2012) diffusivities, as modified by Sur et al. (2024). Given its current uncertain nature and likely transient effects, we do not include semi-convection in any models in this work. The effects of semi-convection could be minimal in Jupiter over evolutionary timescales, as observed by Müller et al. (2020), but this topic certainly warrants future scrutiny. Each timestep is determined to ensure the temperature, helium fraction, and heavy-element fraction do not change in a zone by more than 1% and 750 spatial zones are employed. All models in this work conserve cumulative energy to within 1%, using Equations 58 and 59 in

Sur et al. (2024). We conducted resolution tests with mass zones spanning 250 and 1000 zones and temporal resolution between 0.5% and 5%. We find that models with more mass zones and temporal resolution require significantly more computing time than we suggest is warranted by the corresponding modest improvement in energy conservation ($\sim 0.2\%$).

3. PRESERVATION OF INITIAL HEAVY-ELEMENT EXTENDED CORES

This section explores the general contexts in which an extended "fuzzy" Jovian core of heavy elements might survive until the present day. As illustrated in the bottom panel of Figure 1, the range of fuzzy core structures inferred from the *Juno* data is quite broad. Debras & Chabrier (2019), Militzer et al. (2022, MH22), and Militzer & Hubbard (2024, MH24), infer flat Z profiles out to a steep Z gradient near ~ 0.6 R$_J$, where R$_J$ is the radius of Jupiter. If composition profile gradients are overrun by convection, they will then be mixed and will not survive over Gyr timescales. A narrow Z gradient, flanked by flat interior and exterior profiles, presents a physical challenge, since such a configuration would naturally arise only under conditions of homogenizing convection. A fully convective, adiabatic initial envelope, which would homogenize the planetary structure, is inconsistent with the presence of a fuzzy core. Therefore, we initialize the envelope as stably stratified, imposing an initial positive entropy gradient to achieve this. Hence, we investigate the general conditions under which convection can be suppressed, allowing a fuzzy core and its associated stabilizing Z gradients to persist.

In §3.1 we explore how a class of initial steep Z profile gradients in the middle of the planet surrounded by flat Z distributions might survive Gyr timescales of thermal, structural, and compositional evolution. In §3.2, we explore the dependence of the Z profile gradient on internal entropy profiles by varying from cold to hot internal entropies. The initial models in §3.1 and §3.2 are constructed with linear profiles along the mass coordinates of the structure. For each model, there are two flat linear profiles surrounding a steep linear heavy element profile. We maintain three linear, piecewise profiles for the entropy, but introduce slopes in the regions of flat Z profiles to sustain a fully stable initial condition. We present these models graphically in Figures 2–5. This is followed in §3.3 by an investigation into how fuzzy cores with a different class of initial Z profiles which gradually decrease in Z abundance from the inside out might fare over time. This different class of initial conditions resembles the more smoothly continuous present-

day Jovian Z distributions inferred by Nettelmann et al. (2021). We emphasize that we are not directly addressing in this study planet formation scenarios that might produce such profiles.

All the models explored in §3.1–§3.3 are given a total heavy-element mass of 27 M$_\oplus$. The choice of 27 M$_\oplus$ for these "flat-top" experiments are motivated by the recent suggestions of Militzer & Hubbard (2024), who found that a total heavy element mass of 27 M$_\oplus$ is consistent with their flat-top fits to the Juno data. Nevertheless, any heavy element total mass would demonstrate the effects shown in §3.1 and §3.2.. Of this total, 2.5 M$_\oplus$ are put in a compact core made up of 50% water and 33.33% post-perovskite (MgSiO$_3$), with the remainder iron using the EOS used in Zhang & Rogers (2022), which is Keane's EOS (Keane 1954; Stacey & Davis 2004) expanded to high pressures and temperatures for this work. For simplicity, water is the only heavy species in the envelope. Furthermore, all initial models assume an initial constant helium abundance relative to hydrogen at the protosolar value of $Y' = Y/(X + Y) = 0.277$, as calculated by Bahcall et al. (2006).

3.1. *The Survival and Consequences of Flat-Top Fuzzy Cores*

The initial heavy metal (Z) and entropy (S) profiles presented in this section follow the same general trends recently found by Knierim & Helled (2024). Namely, that initial Z profiles located at larger radii convectively mix[1] more rapidly than those located deeper in the structure. From left to right, Figure 2 depicts what happens when the initial location of the steep gradient is moved progressively outward. The convective zones move inward, and these zones convectively mix the extended cores, as shown in the second row of Figure 2. Models that mix throughout access all the heat of the envelope, leading to higher effective temperatures. In Figure 3, we show that the models with larger extended cores experience lower effective temperatures due to inefficient heat transport from their interiors at early times. The model with its initial fuzzy core extending out to 0.4 M$_J$ (shown in blue) can hold its extended core over Gyr timescales and shows higher effective temperatures at early times since it can access more of this interior heat. The evolution of the equatorial radius is shown in the bottom panel of Figure 3. These example models illustrate the dependence of the effective temperature on the initial Z and S profiles. The 0.4 M$_J$ model in Figure 3 reaches the current Jovian effective temperature at $\sim$3 Gyrs,

---

[1] Our working definition of "mixing" are regions where $\partial Z/\partial m = 0$.

and its extended core is preserved only by narrow stable regions enclosed by convective regions with no extended stable zone. The convective regions can penetrate the Z profile gradient when the entropy profile of the outer region cools to lower values close to those of the innermost stable region of the model. Our evolution profiles show so-called "staircases," also observed by Vazan et al. (2018) and Müller et al. (2020). Stellar evolution codes, such as MESA (Paxton et al. 2011, 2013) also exhibit similar staircase behavior (see Figure 2 of Paxton et al. 2018). They are not expected to occur in Nature, are not observed in 3-D hydrodynamic simulations, and are not the same as those expected by semi-convection or double-diffusive convection (Leconte & Chabrier 2012; Wood et al. 2013; Moll et al. 2017; Tulekeyev et al. 2024). The models in this section are not representative of Jupiter's evolution, and for demonstration purposes only, we have used the unmodified LHR0911 miscibility curve, shown in the bottom row of Figure 2.

3.2. *The Consequences of Initial Entropy*

Initial fuzzy cores with higher (or "hotter") S profiles mix more rapidly due to convection than those with lower (or "colder") S profiles (Müller et al. 2020; Knierim & Helled 2024). From left to right, Figure 4 illustrates this dependence of the Z profile on the S profile. The location of the Z profile is maintained in Figure 4 at 0.6 M$_J$ to illustrate the S profile effects on the Z profile. To guide the eye, a characteristic entropy at the position of the Z gradient (ranging from 6.5 to 8.5 k$_B$ baryon^{-1}) is marked by black dash-dot lines in the first row. The inward advancement of the convective front is inhibited by the Z gradient in colder S profiles, causing the outer convective regions to cool more rapidly without heat replenishment from the interior. This outer adiabatic cooling results in lower effective temperatures and smaller radii, as shown in Figure 5. As outer temperatures drop, they intersect the shifted SR18 miscibility curve, as shown in the left-most column. As such, preserving these extended cores results in effective temperatures much colder than the present-day Jovian effective temperature. As in the previous section, and since these are only example models, we arbitrarily increased the demixing temperatures of the SR18 miscibility curve by +550 K for these example calculations.

3.3. *The Survival and Consequences of Gradually Sloping Fuzzy Cores*

The shortcomings and challenges of the profiles explored in §3.1 and §3.2 motivate the exploration of a different kind of initial distribution. The reader should keep in mind that although formation models have pro-

vided initial conditions to be used in evolutionary models, these have not in the past been shown to preserve fuzzy cores larger than $\gtrsim 0.2$ M$_J$ (Müller et al. 2020). Based on our example evolution models described in §3.1 and §3.2, initially steep Z profile gradients extending beyond 0.4 M$_J$, as advocated in the models of MH24, do not seem at the same time to easily explain the Jovian effective temperature in an evolutionary context. Those initial Z distributions which have an initially stable interface at interior masses greater than 0.5 M$_J$ mix too rapidly to provide a stable Z region at the present age, as shown in Figure 2. If such a profile is initialized with colder interior entropy profiles, then the stable Z region will endure (Figure 4). The outer regions, though, will cool rapidly and fail to account for Jupiter's current effective temperature, as illustrated in Figure 5. These colder models can be provided with higher exterior entropy profiles to achieve higher initial effective temperatures. Although such models experience higher initial effective temperatures, they nonetheless cool to effective temperatures below 120 K at later ages. One may believe that this problem might be alleviated with higher initial internal temperatures near the steep Z gradient, but the associated elevated internal entropies will mix the profile gradients, as demonstrated in Figure 4. A negative Z gradient can be introduced interior to the steep portion of the profile to keep the extended core from fully mixing. This maintains the extended core out to 0.5 M$_J$, but the effective temperatures remain below 120 K at 4.56 Gyrs. The requirement to maintain the steep Z gradient at $M \sim 0.5$–0.6 M$_J$ conflicts with the need to sustain high enough temperatures in the convective region to achieve an adequate $T_{\rm eff}$ for this kind of profile. Thus, while a steep Z profile gradient can persist over Gyr timescales under certain conditions, we disfavor such initial configurations due to the requirement to match Jupiter's effective temperature.

Facing these challenges, we explored a more gradually sloping class of initial conditions. The exercise in §3.2 is repeated in Figures 6 and 7, where the initial fuzzy cores are instead gradual throughout the inner envelope. The unmodified miscibility curves of LHR0911 have been used to illustrate helium rain in these example models. As in Figure 4, Figure 6 depicts models for which a characteristic entropy (shown in the first row) ranges from 6.5 to 8.5 k$_B$ baryon^{-1}, demonstrating the effect of the gradual increase of the S profile from left to right. The rightmost model described by the highest entropy mixes completely by 0.4 Gyr, while the others maintain their extended fuzzy cores to varying degrees. In Figure 7, we show that the gradual core evolutionary model characterized by 7.5 k$_B$ baryon^{-1}(third column),

which indeed preserves a stable fuzzy core, can reach an effective temperature closer to that of Jupiter. This class of initial conditions allows for a more gradual evolution of the effective temperature (see Figure 7). As shown in Figure 6, internal entropies of between 7 and 7.5 k$_B$ baryon^{-1}appear adequate for this kind of initial condition.

Initial internal entropies of 7.5 kb/baryon are in contrast to past "hot-start" gas giant models. Recently, Müller et al. (2020) explored hot (~ 9 k$_B$ baryon^{-1}) interior entropies along with cold (~ 7 k$_B$ baryon^{-1}) formation models of Jupiter and evolved them to the present epoch. The "Cold extended" model of Müller et al. (2020) and the cold models of Cumming et al. (2018) have entropy profiles consistent with our own. The cold profiles of Cumming et al. (2018) and Müller et al. (2020) both have ~ 7 k$_B$ baryon^{-1} in their deep stable regions, as do ours. We note that depending on the initial entropy profile, the outer entropy can gradually rise to entropies reminiscent of the older "hot-start" models, close to 9-12 kb/baryon. However, these rapidly (< 10 Myr) cool to entropies below 8 kb/baryon. Such an initial entropy distribution can be considered a hybrid of cold and hot start models.

4. EVOLUTION OF JUPITER

To find a favored model with the class of initial conditions discussed in §3.3, we conducted a parameter search by varying the total mass of heavy elements, M$_z$, from 25 M$_\oplus$ to 50 M$_\oplus$. For each M$_z$, the compact core mass (M$_c$) was varied from 2 to 15 M$_\oplus$. The ranges of total heavy element masses and compact core masses are motivated by the lower and upper mass limits allowed by the Juno gravity data (see Figure 3 of Wahl et al. 2017). For each of these models, we varied the miscibility temperature modifications (ΔT) from -500 K to 500 K (for LHR0911) and from 0 K to 2,500 K (for SR18). Figures 2–7 show that internal characteristic entropy values of 7.5 k$_B$ baryon^{-1} strike a balance between preserving an extended core and yielding appropriate effective temperatures for Jupiter at the present age. Thus, each model was initialized with a characteristic interior entropy of 7.5 k$_B$ baryon^{-1}and an outside entropy of 8.2 k$_B$ baryon^{-1}. Although a wide variety of initial profile distributions could be constructed and brought close to matching observed data, this particular class of initial Z distributions is naturally suited to match the observables presented in Table 1. Specifically, it preserves an inner stable region better and provides enough erosion of the extended core via convective mixing to obtain a metallicity of $3Z_\odot$ in the outer regions.

Our preferred model for Jupiter's evolution is presented in Figures 8 and 9. The observed parameters of this model are compared to the data for Jupiter in Table 2. The relative errors of this model's effective temperature and radius are within 0.05% and 0.2% respectively, all while Y_{atm} reaches the value of 0.234. In this model, helium rain begins at 4 Gyrs. Importantly, the miscibility temperatures required to achieve $Y_{\text{atm}} = 0.234$ are +300 K higher than the original LHR0911 immiscibility temperatures. At the same time, a significant temperature modification of +2,200 K to the SR18 miscibility curve is required. The required miscibility curves of LHR0911 and SR18 are compared to the original model in Figure 10, with experimental H-He phase separation data from Brygoo et al. (2021) interpolated and plotted for comparison. Our prediction of a higher miscibility temperature falls within 3σ of the Brygoo et al. (2021) experimental results. The elevated immiscibility temperatures are in part a result of the higher profile temperatures in the convective regions due to the presence of heavy metals in the envelope. The difference seen in Figure 10 between the shifted LHR0911 and SR18 miscibility curves is a consequence of their different shapes in the $\sim 1-4$ Mbar pressure region of relevance to helium rain in Jupiter. A recent evolutionary calculation that incorporates only H-He in the interior of Jupiter's envelope predicts colder demixing temperatures, by as much as -1,250 K concerning the original LHR0911 miscibility curve (Howard et al. 2024). The best-fit Jupiter model of Mankovich & Fortney (2020) seems to have a homogenous envelope metallicity of only $\sim$one solar, with the correspondingly lower envelope temperatures and lower required shift to the SR18 miscibility curve. We conclude that the inclusion of heavy metals in the envelope results in higher temperatures and, therefore, warrants higher H-He demixing temperatures.

Our preferred Jupiter model is the first to incorporate the evolution of initially stable extended cores to match the effective temperature, radius, outer metal abundance, and atmospheric helium abundance with helium rain within reasonable uncertainties. One of the subsidiary conclusions we draw from the explorations in §3.1 and §3.2 is that steep Z profile gradients surrounded by flat Z profiles left over from formation will lead to effective temperatures that are too low for the present Jupiter. This is due to the lack of heat resupply from the interior, since heat transport in these stable regions relies on conduction, which is significantly less efficient than convection. As a result, stable regions located between 0.4 M$_J$ and 0.6 M$_J$ severely inhibit heat transport.

Since the aim of this study was to investigate which initial distributions 1) can retain extended stable cores and 2) can account for Jupiter's effective temperature, atmospheric helium abundance, and equatorial radius, we chose initial distributions better suited for that purpose. Past evolutionary models informed by formation models have thus far been unable to reproduce the inferred *Juno* Z profiles (Müller et al. 2020; Stevenson et al. 2022). The evolutionary models of Vazan et al. (2018) end with an extended core region out to 0.38 M$_J$ but did not attempt to impose the constraint of the measured atmospheric helium abundance, used the older SCvH EOS (Saumon et al. 1995), and did not employ an up-to-date atmospheric boundary. The stable region predicted by the formation and evolutionary models of Müller et al. (2020) extends to only 0.2 M$_J$. More recently, Howard et al. (2023a) investigated the H-He EOS dependence of static Jupiter models, also favoring an extended core out to 0.2 M$_J$. The evolutionary models presented in our work begin with a completely stable structure but also end with an extended core region out to $\sim$0.3 M$_J$.

Our work is distinguished from the works of Vazan et al. (2018), Müller et al. (2020), Mankovich & Fortney (2020), Howard et al. (2024) in the following ways:

1. The use of updated boundary conditions which account for irradiation, the Bond albedo, and ammonia clouds (Chen et al. 2023). These boundary conditions are Y-dependent, adjusting to the outer Y abundance during helium rain.

2. The use of an updated H-He EOS (Chabrier & Debras 2021) and the incorporation of a multiphase water EOS (Haldemann et al. 2020).

3. An exploration of different classes of initial condition profiles for S and Z. The various initial conditions explored by Müller et al. (2020) were formation models, whereas here we have explored the evolutionary consequences of the flat-top profiles and smooth profiles in the thermal evolution of Jupiter.

4. The application of the two most recent H-He miscibility curves (LHR0911, SR18) used in the evolution of Y in the presence of Z profile gradients. These H-He miscibility curves are allowed to adapt and adjust to the local pressures, temperatures, and helium abundance.

5. The deployment of a new evolutionary code (APPLE ; Sur et al. 2024) with updated microphysics, such as conductivities, helium rain mod-

eling methods, and the inclusion of centrifugal effects on the structures.

5. CONCLUSIONS

Generally, the Z profiles that retain stable regions are deeper in the planet (≤ 0.4 M$_J$) compared to those inferred by DC19, MH22, and MH24 and must begin with a characteristic interior entropy of $\sim$7.5 k$_B$ baryon^{-1}, which is compatible with cold-start formation models (Cumming et al. 2018; Müller et al. 2020). Lower interior entropies lead to colder outer temperatures, and higher interior entropies lead to more convective mixing (see Figure 4). In addition, metallicity profile gradients surrounded by flat profiles located at $\gtrsim 0.4$ M$_J$ will either convectively mix or lead to effective temperatures significantly colder than 125 K. Including a stabilizing region interior to the steep profile gradient leads to a more stable core but aggravates the fit with effective temperature. As a result, initial Z distributions with steep stable profile gradients located in the outer regions (M ≥ 0.6 M$_J$) may not be the result of formation processes.

Obtaining $\sim 3 Z_\odot$ metallicity in the outer envelope leads to higher temperatures in the outer convective region since (generally) higher metallicity temperature profiles are significantly hotter than pure H-He profiles. As a result, to deplete sufficient helium from the atmosphere, significantly higher H-He demixing temperatures are required. In this work, the LHR0911 and SR18 miscibility curves require higher temperatures by $\sim$300 K and $\sim$2200 K, respectively.

While the observed metallicity of Jupiter's atmosphere may be due to recent impact events (see discussions in Debras & Chabrier 2019; Helled et al. 2022), it remains unlikely that positive Z profile gradients will remain stable over even megayear timescales. As such, we have assumed here that the atmospheric metallicity of Jupiter is the same throughout the outer convective region.

We emphasize that the fits to the *Juno* gravity data constrain only the mass density profile in the current Jupiter. The interior thermal distributions are not constrained at all and are therefore assumed by all researchers attempting to use the *Juno* gravity data. This accounts for the wide range of inferred density distributions and forcefully suggests that the interior thermal profiles are very much unconstrained. This is where evolutionary models can play a useful role. Since they fundamentally depend upon the thermal interior and the associated energy transport model, they bring to bear other constraints, such as the atmospheric effective temperature at the current epoch. They also can connect the formation phase with the current phase, something

Nature does and theorists should attempt. However, our current models shed little light on Jovian birth, other than to constrain the possible character of a fuzzy core at formation, if that measured extended core is primordial.

We have left to future work attempts to fit in the context of evolutionary models the current *Juno* lower-moment (J_2 and J_4) gravity data (Sur et al. 2024 b, *in prep.*). This is in part due to the difficulty researchers have had fitting them in the context of Jupiter's measured surface metallicity (Nettelmann 2017; Nettelmann et al. 2021; Helled et al. 2022). Such static fits to *Jupiter* (see Figure 1) seem often to require low metallicities, and sometimes negative metallicities (Nettelmann et al. 2021) in the outer envelope. Debras & Chabrier (2019) has proposed a positive Z gradient in the outer regions of Jupiter (red line in the bottom panel of Figure 1) while Howard et al. (2023b) find that a positive Z gradient of such magnitude requires an excessive amount of late accretion inconsistent with collisional evolution models of the Solar System. On the other hand, Müller & Helled (2024) argue that a possible reduction in local opacity in the deep atmosphere could form a stable layer even in the presence of a destabilizing Z gradient shortly after formation, allowing the upper atmosphere to be enriched by collisions, while the deep interior remains metal poor.

As proposed by Stevenson (1982), core erosion could be responsible for generating Z gradients and fuzzy cores on evolutionary timescales, and core erosion will be a subject of future work. We have not in this paper incorporated the potential effects of semi-convection and semi-convective interfaces (Moll et al. 2016, 2017; Fuentes et al. 2022; Tulekeyev et al. 2024) that have been shown to endure over evolutionary timescales in the presence of rotation (Hindman & Fuentes 2023; Fuentes et al. 2023, 2024), though Müller et al. (2020) found they had no significant effect without rotation. Clearly, the effects of both rotation and semi-convection require further scrutiny.

Uncertainties exist in the hydrogen-helium and heavy-element equations of state, the H-He demixing temperatures and pressures, and in other material properties at high pressures that render both evolutionary and static models provisional. In the context of the high Zs inferred in current models, the lack of physically sophisticated equations of state for hydrogen/helium/heavy-element mixtures for the range of compositional mixtures discussed in the literature is a particularly important shortcoming of all current models of Jupiter (and Saturn).

Despite all these uncertainties, evolutionary models are crucial for determining the long-term stability of these fuzzy cores in the presence of convective mixing, in informing formation models, and in clarify what evolutionary paths are feasible, given the various observational constraints. Their continued development and refinement are key to the eventual understanding of this class of planet, whose importance extends beyond the Solar System giants to the giant exoplanets now being discovered in profusion and that await a definitive understanding of our local variants.

Figure 2. Example evolutionary calculations of four mock models with varying initial sizes of the extended core. From left to right, the models increase in extent from 0.4 to 0.8 M_J. All models have a total envelope heavy-element mass of 27 $M_\oplus$ with 2.5 $M_\oplus$ in the compact core ($Z = 1$). The four models in this study assume the same initial entropy of 7.5 k_B baryon^{-1} at the outer edge of the fuzzy core but shift in location to match the location of each stable region. The surrounding flat Z profile regions have been initialized with stabilizing S profile gradients. None of these models should be taken as the preferred models of Jupiter. Rather, these models are meant to explore the contexts for the survival of the given fuzzy cores to late times. Since these are example models only, we have used the original LHR0911 miscibility curves to demonstrate helium rain. The first row depicts the entropy profile and the inward extension of the convective zone as each structure cools. At later ages, when the outer region has cooled more than the inner stable region, the convective zones surround the steep stable regions, leaving behind so-called "staircases" (see also Vazan et al. 2018). The second row shows the evolution of the Z profile. Generally, these figures show that shallower (i.e., located closer to the surface) extended cores experience more convective mixing than deeper extended cores. The third row shows the evolution of the helium abundance profile. Due to the conservation of mass and the setting of the hydrogen/helium mass ratio equal to the proto-solar value ($Y/(X + Y) = 0.277$; Bahcall et al. 2006), the helium abundance increases with decreasing heavy metal abundance. The last row shows the evolution of the temperature profile with the helium rain region of the 0.4 M_J model shaded in red. Note that all but the 0.4 M_J model mixes entirely by 4.56 Gyrs. As a result, the temperatures in the convective envelope of the 0.4 M_J model are colder than the rest at this age. At early ages, however, the temperature profiles of this model are higher than the rest, since it can access more internal heat due to a deeper stable region. Deeper extended cores allow more heat to be available to the outer convective zone and this maintains higher outer envelope temperatures.

Table 2. Jupiter Data vs. Derived Evolutionary Model

Parameter	Value	Derived Model Values
T_{eff} [K]	125.57 ± 0.07	125.44
Y_{atm}	0.234 ± 0.005	0.234
Z_{out} [$Z_\odot$]	~ 3	3.26
Equatorial Radius [km]	$71,492$	$71,697$

NOTE—Jupiter observable data compared to the values of our preferred model from §4 at 4.56 Gyrs. This particular model has a total heavy element mass of $M_z = 44\ M_\oplus$ and a compact core mass of $M_c = 14\ M_\oplus$ and uses the LHR0911 miscibility curve with a demixing temperature modification of +300 K to reach the observed helium mass fraction of 0.234.

Table 3. H-He Miscibility Temperature Shifts

Authors	Misc. Curve (ΔT)
This Work	LHR0911, SR18 (+300 K, +2200 K)
Howard et al. (2024)	LHR0911, SR18 (−1250 K, +350 K)
Mankovich & Fortney (2020)	SR18 (+539 K)
Mankovich et al. (2016)	LHR0911 ($\lesssim -100$ K)
Püstow et al. (2016)	LHR0911 (+500 K)
Nettelmann et al. (2015)	LHR0911 (+250 K)

NOTE—List of H-He miscibility temperature shifts in the literature needed to match helium abundance observations of Jupiter and Saturn. The temperature shifts of this work as a result of evolving stably stratified Z profiles are provided in the first row. We note that the experimental results of Brygoo et al. (2021) show a demixing temperature of H-He that is $\sim$7000 K higher than the SR18 demixing temperatures and $\sim$3000 K higher than the LHR0911 demixing temperatures at megabar pressures.
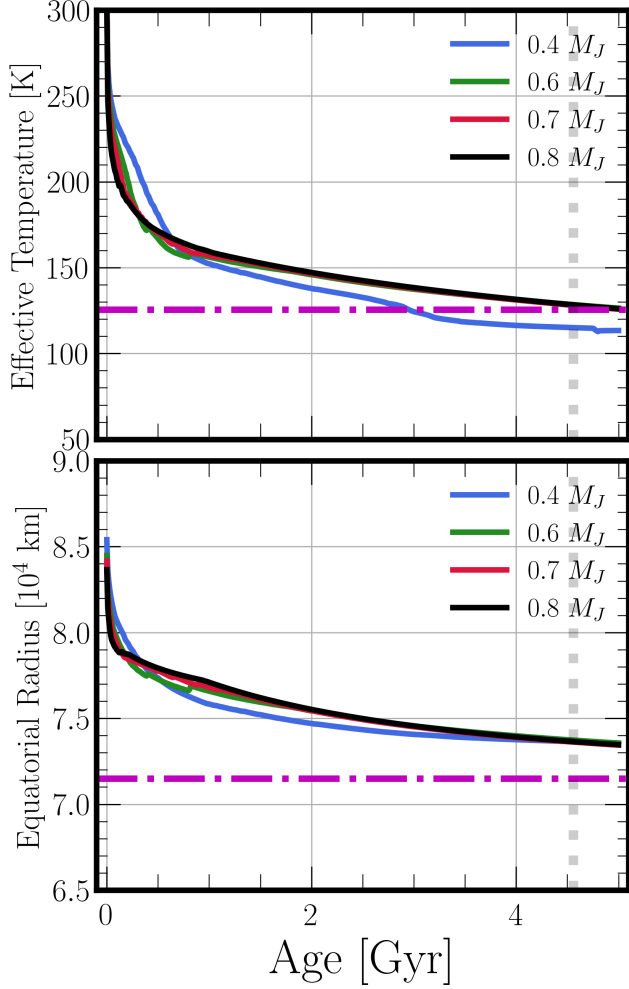
Figure 3. Effective temperature (top panel) and equatorial radius (bottom panel) evolution of the models presented in Figure 2. The models are distinguished by the initial extent of the stable regions corresponding to the columns in Figure 2. The deepest fuzzy core model, 0.4 M$_J$, accesses more heat than other models at early times. At later times, however, this model still cannot efficiently access interior heat, while the other models have convectively mixed and, thus, their interior heats are made available to their exteriors. The effective temperature of this model, therefore, is higher than those of other models at early times, but lower at later times. The violet horizontal line in the top panel marks the observed effective temperature of Jupiter of 125.57 K (Li et al. 2012) and the equatorial radius in the bottom panel, as measured by (72,492 km; Seidelmann et al. 2007). Due to the high interior temperatures, the radii remain larger than the equatorial radius of Jupiter in these mock evolutionary models. The purpose of Figure 2 and this figure is not to obtain the correct radius (for that, see §4 and discussions thereafter), but rather to illustrate that only extended stable regions located at ≲ 0.4 M$_J$ can maintain a semblance of a stable region.
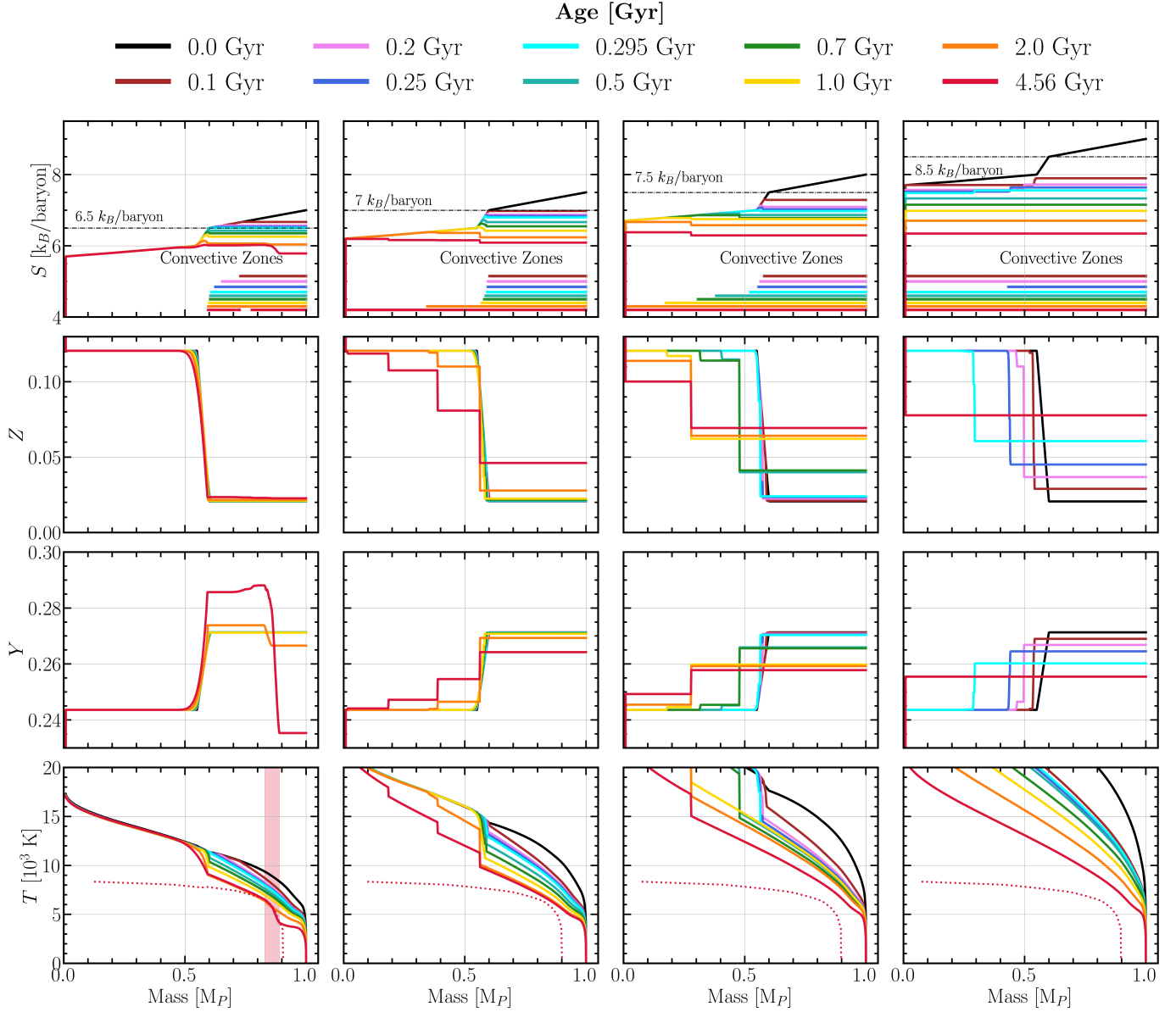
Figure 4. Example evolution models of four mock models with varying initial entropy profiles, increasing from low entropy (left column) to high entropy (right column). These models were initialized with a steep Z profile gradient surrounded by flat Z regions, but are provided with stabilizing S profile gradients on either side. To observe the effect of varying the overall entropy profile, these models all begin with the same Z profile, with a steep gradient fixed initially for all models at 0.55-0.6 M_J. From left to right, this figure shows that higher internal entropies destroy the initial Z profile gradients. As a result of their lower initial entropies, those that survive experience colder temperatures in the convective region. The first row shows the inward-moving convective zones as each model cools. The second row shows the evolution of the Z profile. Even a modestly cold initial interior entropy of 7.5 k_B baryon^{-1} can convectively mix an initially stable region at this location (0.6 M_J). Higher interior entropies mix the Z gradients to varying degrees, with the last model on the left mixing completely in under 200 Myr. The third row depicts the evolution of the helium abundance (Y) profile, including helium rain, where we have modified the demixing temperatures of the SR18 miscibility curves by +550 K for example purposes only. Due to conservation of mass and the setting of the hydrogen/helium mass ratio equal to the protosolar value, regions of high Z correspond to regions of low Y, and vice-versa. The last row shows the temperature profiles with the helium rain region shown as the red shaded region. The two coldest models shown in the left-most columns experience less convective mixing over evolutionary timescales, and their outside regions are therefore allowed to cool without constant resupply of heat from the interior. This leads to even colder outer temperature profiles, which eventually intersect the miscibility curve employed here (seen in gray). On the other hand, the two hottest models shown in the rightmost columns mix completely and remain hotter throughout their interior leading to higher temperature profiles at later ages.
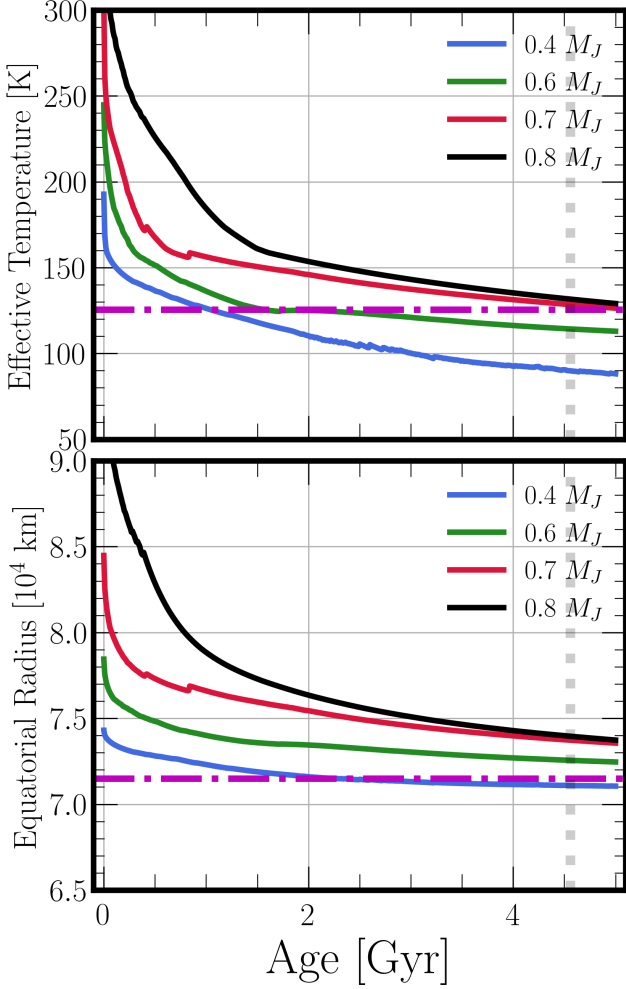
Figure 5. Evolution of the effective temperature (top panel) and equatorial radius (bottom panel) of the four mock models presented in Figure 4. The four models are distinguished by the entropy at the boundary of the fuzzy core corresponding to the columns of Figure 4. The models initialized with higher entropies result in hotter effective temperatures and larger radii since their stable regions are convectively mixed at earlier ages. For example, the model with interior characteristic entropy of 8.5 k_B baryon^{-1} that the black line represents mixes entirely in under 200 Myrs. The red line representing the 7.5 k_B baryon^{-1} model mixes almost entirely by 1 Gyr, after which the effective temperature recovers from its steep initial dive. The discontinuity jumps visible in the red line are due to rapid mixing events of the Z profile. The dotted gray line marks 4.56 Gyr. At later times, the effective temperature of the coldest model (blue line; 6.5 k_B baryon^{-1}) has cooled to under 100 K with a smaller radius than the rest of the models. This model was initialized with colder interior temperatures and thus did not convectively mix. Its convective region therefore evolved without heat resupply from the interior leading to low temperatures on the outside. The violet horizontal line in the upper panel marks the observed effective temperature of Jupiter of 125.57 K (Li et al. 2012) and the violet line in the bottom panel the equatorial radius of Jupiter (71,492 km; Seidelmann et al. 2007).
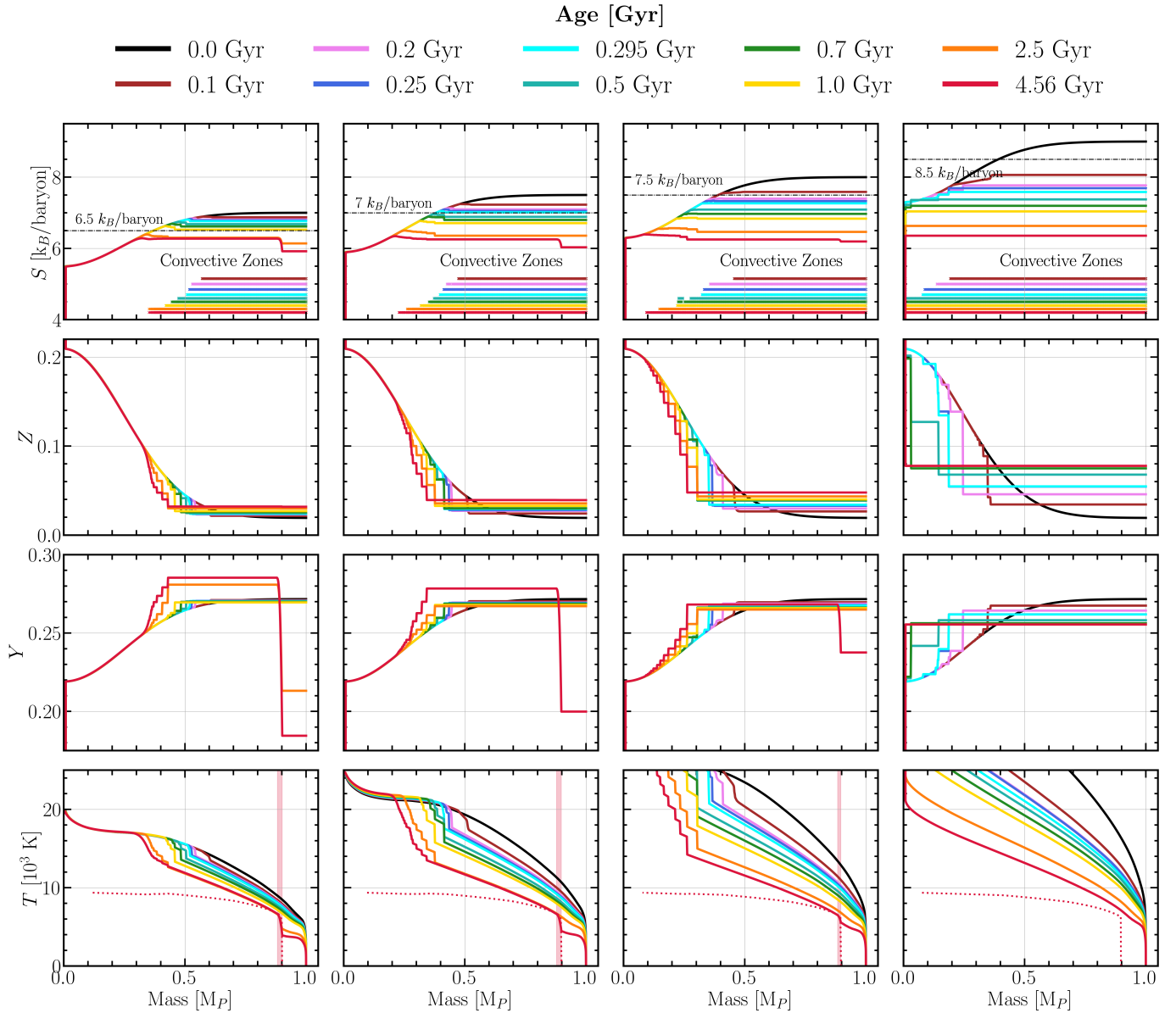
Figure 6. Example evolutionary models with gradually extending cores. This figure follows the exercise conducted in Figure 4, starting at a median low interior entropy of 6.5 k_B baryon^{-1}(left) to high median interior entropy of 8 k_B baryon^{-1}(right). To show helium rain in these models and only for example purposes, we have used here an unmodified LHR0911 miscibility curve. As in all prior figures, the models have a total heavy envelope mass of 27 M$_\oplus$ with a 2.5 M$_\oplus$ compact core. The first row depicts the inward motion of the convective zones as the planet cools. The second row shows the evolution of the Z profile and, importantly, showcases that higher interior entropies lead to rapid convective mixing of the composition gradient. Cooler initial entropy profiles let their outer regions cool at a faster rate without access to heat from the interior, leading to encounters with the LHR0911 miscibility curves at later ages. The third row shows the evolution of the total helium abundance, Y, and its depletion due to helium rain. Given mass conservation, regions of higher heavy element abundance correspond to regions of lower helium abundance. The last row shows the evolution of the temperature profile and the helium rain region is shaded in red. Compared to the models presented in Figure 4, these initial conditions keep the convective zones from moving to the deep interior regions, leading to stable regions at Gyr timescales, with higher metal abundances in the exterior without mixing completely.
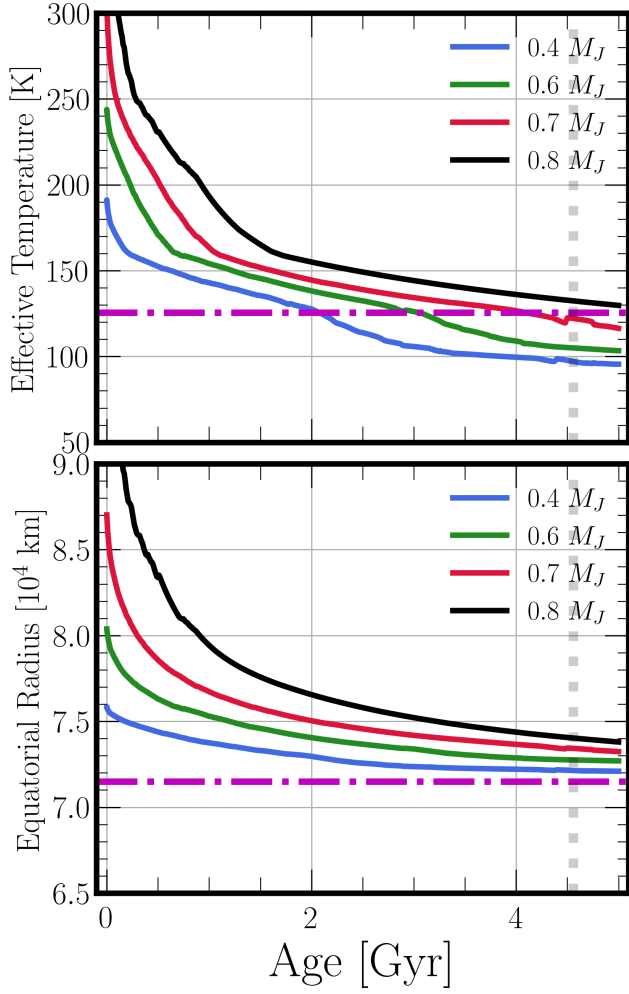
Figure 7. Evolution of the effective temperature (top panel) and radius (bottom panel) of the four models presented in Figure 6, denoted by the corresponding median internal entropies corresponding to the columns of Figure 6. The dotted gray line marks 4.56 Gyrs. Unlike the models in Figure 4, the initial distributions of S and Z allow for a more gradual evolution of the effective temperature even for the 7.5 k_B baryon^{-1}model, represented by the red curve. This model retained a stable region out to 0.35 M_J, and came closer to Jupiter's effective temperature. The magenta line in the top panel marks the observed effective temperature of Jupiter of 125.57 K (Li et al. 2012) and the equatorial radius of Jupiter (71,492 km; Seidelmann et al. 2007) in the bottom panel.
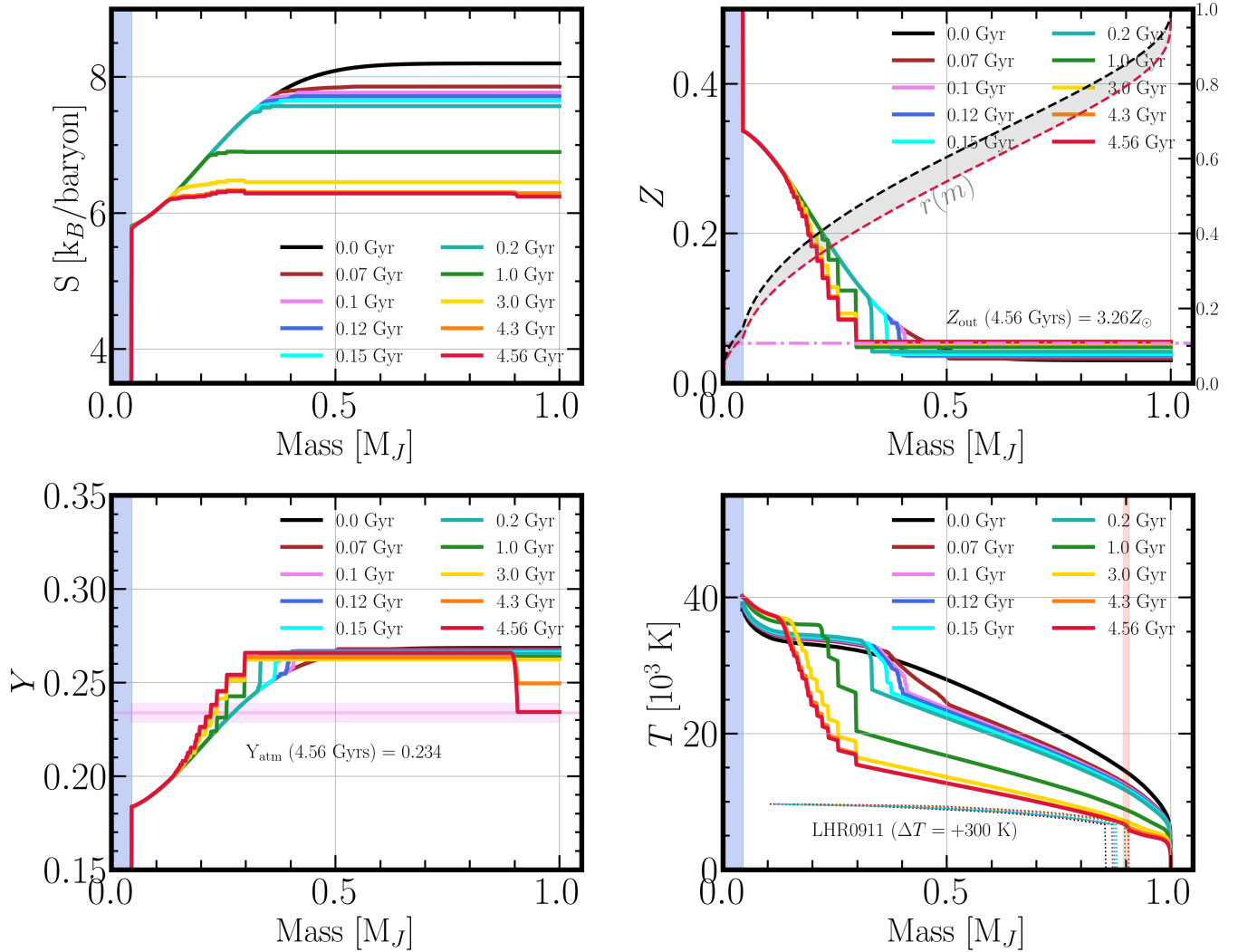
Figure 8. Evolutionary model to the present-day that best matches the effective temperature, radius, atmospheric helium abundance, and outer envelope metallicity within observational uncertainties. The initial mean entropy per baryon is 7.5. The top left shows the evolution of the entropy profile, the top right the evolution of the composition (Z) profile, the bottom left the evolution of the helium (Y) profile, and the bottom right the evolution of the temperature profile. This particular model contains a total of 44 $M_\oplus$ of heavy elements with a 14 $M_\oplus$ compact core ($Z = 1$), marked by the shaded blue regions. As shown in the upper right panel, the initial Z profile becomes convectively mixed from the outside toward the inside, and this change is most pronounced at early times. The dark-shaded region represents the normalized radius as a function of normalized mass, whose coordinates are on the second Y-axis and whose boundaries are color-coded according to the initial and final age. The resulting extended core ($dZ/dm < 0$) extends out to 30% of the planet's mass, corresponding to 42% of the radius at 4.56 Gyrs. The outer metallicity begins at $1.5 Z_\odot$ and rises to 3.26 $Z_\odot$. Regions of higher metallicity correspond to regions of lower helium mass fraction. Helium rain begins at 4 Gyrs in this model, for which we use the LHR0911 miscibility curves with a temperature shift of +300 K to deplete the helium in the outer layers to 0.234. The latter is consistent with the *Galileo* entry probe measurements (Von Zahn et al. 1998). The demixing temperatures encountered by the temperature profile are shown in the last panel. The dotted lines in the last panel show the adjustment of the LHR0911 miscibility curves to their corresponding temperature and pressure profiles. The long-shaded region corresponds to the helium rain region.
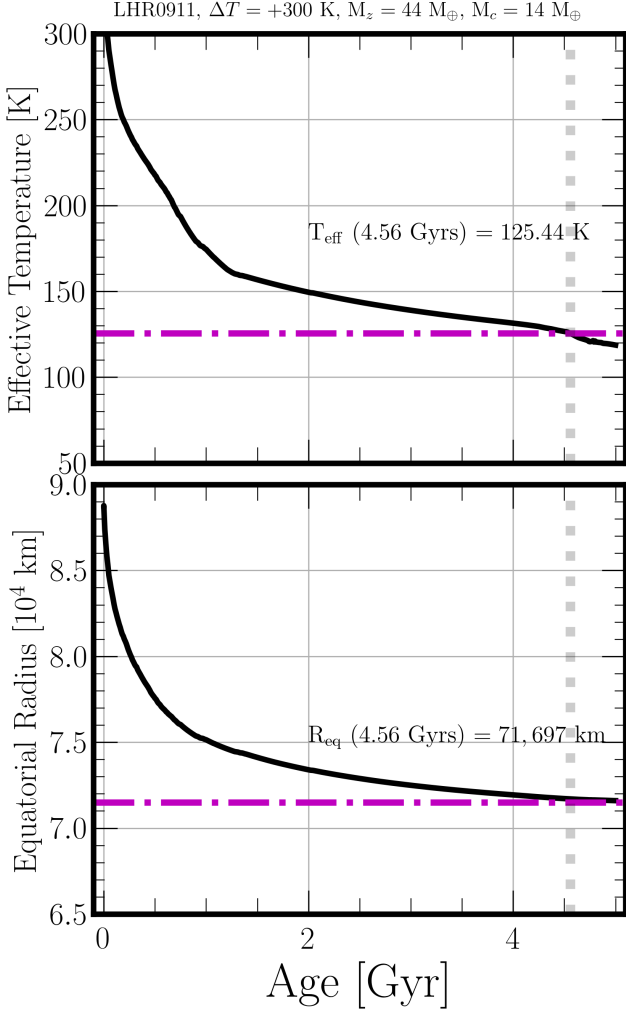
Figure 9. Evolution of the effective temperature (top panel) and equatorial radius (bottom panel) of the preferred evolutionary model of Jupiter in Figure 8. In the top panel, the model reaches the observed effective temperature of Jupiter (125.57 ± 0.07 K; Li et al. 2012) to within 0.06 K (0.05%) of the observational uncertainty. The effective temperature of Jupiter is shown as the horizontal magenta line in the top panel. This model comes to within 0.2% of the equatorial radius of Jupiter (71,492 km; Seidelmann et al. 2007) at 4.56 Gyrs. The values of Jupiter compared to those of this model are provided in Table 2. The equatorial radius is shown as the dash-dot magenta line in the bottom panel.
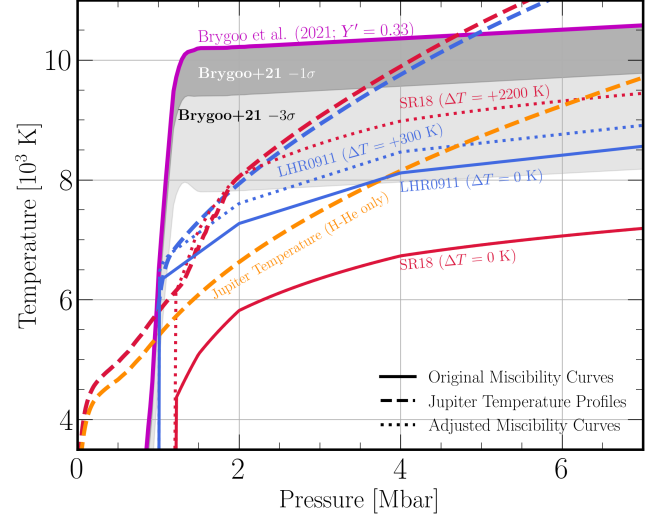
Figure 10. Comparison of the original LHR0911 and SR18 miscibility curves (solid lines) with two Jupiter temperature profiles at 4.56 Gyrs, including the effects of the inclusion of heavy elements in the EOS. The low-pressure demixing temperatures of the SR18 miscibility curves have been limited to 1.2 Mbar and those of LHR0911 to above 1 Mbar. The dotted blue curve depicts our favored model using the LHR0911 miscibility curve, the dotted red curve is a similar model to the SR18 miscibility curve, and the dashed yellow model is a fiducial H-He homogeneous Jupiter profile model. At this age, the outer envelope has a Z of ~3.3 $Z_\odot$, making the temperatures significantly higher compared to those of a $1Z_\odot$ model and more so when compared with the pure H-He model (dashed yellow). These higher temperatures at 4.56 Gyrs motivate the need for higher miscibility temperature modifications compared to the recent H-He models of Mankovich & Fortney (2020, +539 K, SR18) and Howard et al. (2024, -1250 K, LHR0911; +350 K, SR18). The interpolated experimental result of Brygoo et al. (2021) is shown in magenta for comparison. The darker and lighter shaded region highlights the lower 1σ and 3σ uncertainties of that experiment, respectively.

APPENDIX

Below, Figure 11 shows example Jupiter profile models at the present epoch with 250, 750, and 1000 mass zones. The size of the staircases is affected by the model spatial resolution. The location and shape of the stable region, however, is not significantly affected by the spatial resolution choice. The choice of time resolution is even less significant than the variations of spatial resolution shown here.
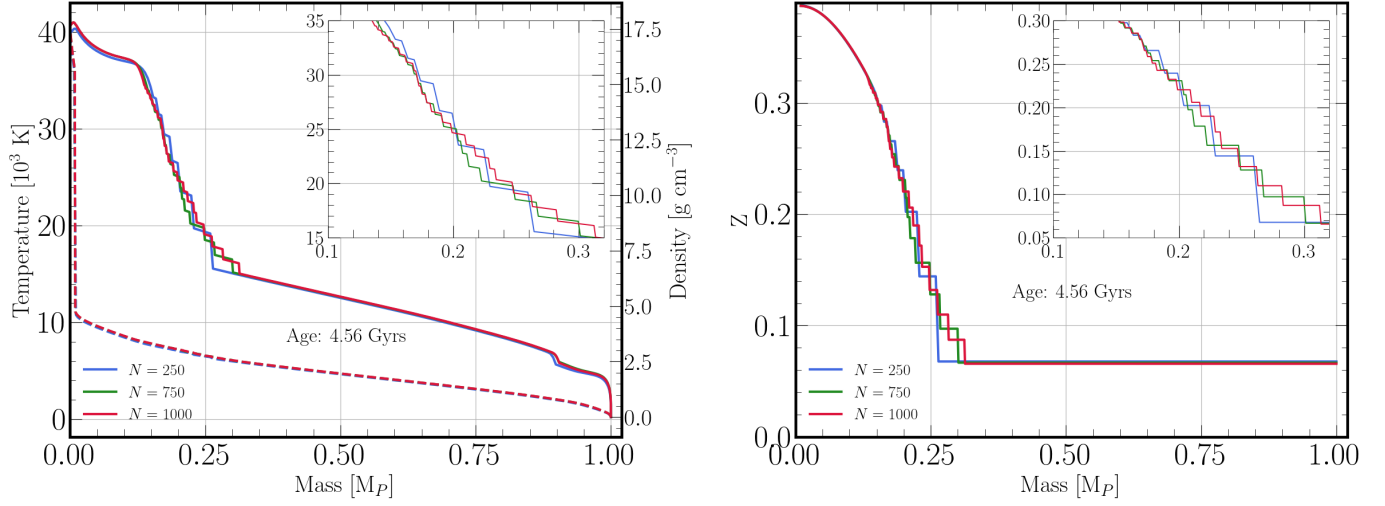
Figure 11. Left: The temperature and density profiles of different models with different spatial resolutions (N) of 250, 750, and 1000 zones, all at 4.56 Gyrs. Right: Heavy metal distribution of the same models at the same age. The inset axes shows the size differences of the staircases. Overall, the number of mass zones used influences the size and number of staircases, but not their location. All models exhibit the staircases at roughly the same Z abundances, and the outer region that experiences homogenization by convection is also of an extent that is independent of the number of zones.

REFERENCES

Bahcall, J. N., Serenelli, A. M., & Basu, S. 2006, The Astrophysical Journal Supplement Series, 165, 400, doi: 10.1086/504043

Bolton, S. J., Lunine, J., Stevenson, D., et al. 2017, Space Science Reviews, 213, 5, doi: 10.1007/s11214-017-0429-6

Brygoo, S., Loubeyre, P., Millot, M., et al. 2021, Nature, 593, doi: 10.1038/s41586-021-03516-0

Chabrier, G., & Debras, F. 2021, ApJ, 917, 6pp, doi: 10.3847/1538-4357/abfc48

Chabrier, G., Mazevet, S., & Soubiran, F. 2019, ApJ, 872, 27pp, doi: 10.3847/1538-4357/aaf99f

Chen, Y.-X., Burrows, A., Sur, A., & Arevalo, R. T. 2023, ApJ, 957, 8, doi: 10.3847/1538-4357/acf456

Cumming, A., Helled, R., & Venturini, J. 2018, MNRAS, 477, 4817, doi: 10.1093/mnras/sty1000

Debras, F., & Chabrier, G. 2019, ApJ, 872, 22pp, doi: 10.3847/1538-4357/aaff65

Durante, D., Parisi, M., Serra, D., et al. 2020, Geophysical Research Letters, 47, 1, doi: 10.1029/2019GL086572

Folkner, W. M., Iess, L., Anderson, J. D., et al. 2017, Geophysical Research Letters, 44, 4694, doi: 10.1002/2017GL073140

Fortney, J. J., Ikoma, M., Nettelmann, N., Guillot, T., & Marley, M. S. 2011, The Astrophysical Journal, 729, 32, doi: 10.1088/0004-637X/729/1/32

French, M., Becker, A., Lorenzen, W., et al. 2012, The Astrophysical Journal Supplement Series, 202, 11pp, doi: 10.1088/0067-0049/202/1/5

Fuentes, J. R., Anders, E. H., Cumming, A., & Hindman, B. W. 2023, ApJ Preprint, 18. https://arxiv.org/pdf/2305.09921.pdf

Fuentes, J. R., Cumming, A., & Anders, E. H. 2022, Physical Review Fluids, 7, 124501, doi: 10.1103/PhysRevFluids.7.124501

Fuentes, J. R., Hindman, B. W., Fraser, A. E., & Anders, E. H. 2024, preprint

Fuller, J. 2014, Icarus, 242, 283, doi: 10.1016/j.icarus.2014.08.006

Fuller, J., Lai, D., & Storch, N. I. 2014, Icarus, 231, 34, doi: 10.1016/j.icarus.2013.11.022

Fulton, B. J., Petigura, E. A., Howard, A. W., et al. 2017, The Astronomical Journal, 154, 109, doi: 10.3847/1538-3881/aa80eb

Gabriel, M., Noels, A., Montalbán, J., & Miglio, A. 2014, A&A, 569, A63, doi: 10.1051/0004-6361/201423442

Gardner, J. P., Mather, J. C., Clampin, M., et al. 2006, SSRv, 123, 485, doi: 10.1007/s11214-006-8315-7

Guillot, T., Fletcher, L. N., Helled, R., et al. 2022. http://arxiv.org/abs/2205.04100

Haldemann, J., Alibert, Y., Mordasini, C., & Benz, W. 2020, Astrophysics A&A, 643, 105, doi: 10.1051/0004-6361/202038367

Helled, R., & Howard, S. 2024, preprint. https://ssd.jpl.nasa.gov/planets/phys_par.html

Helled, R., & Stevenson, D. 2017, The Astrophysical Journal Letters, 840, L4, doi: 10.3847/2041-8213/aa6d08

Helled, R., Stevenson, D. J., Lunine, J. I., et al. 2022, Icarus, 378, 114937, doi: 10.1016/j.icarus.2022.114937

Hindman, B. W., & Fuentes, J. R. 2023, ApJL, 957, L23, doi: 10.3847/2041-8213/ad0642

Howard, S., Müller, S., & Helled, R. 2024, preprint, 1. http://arxiv.org/abs/2407.11120

Howard, S., Guillot, T., Bazot, M., et al. 2023a, A&A, doi: 10.5281/zenodo.7598377

Howard, S., Guillot, T., Markham, S., et al. 2023b, A&A. https://arxiv.org/pdf/2311.07646.pdf

Hubbard, W. B., & Militzer, B. 2016, The Astrophysical Journal, 820, 13pp, doi: 10.3847/0004-637X/820/1/80

Iess, L., Militzer, B., Kaspi, Y., et al. 2019, Science, 364, doi: 10.1126/science.aat2965

Keane, A. 1954, Australian Journal of Physics, 7, 322, doi: 10.1071/PH540322

Knierim, H., & Helled, R. 2024, arXiv e-prints, arXiv:2407.09341, doi: 10.48550/arXiv.2407.09341

Leconte, J., & Chabrier, G. 2012, A&A, 540, 20, doi: 10.1051/0004-6361/201117595

Li, C., Ingersoll, A., Bolton, S., et al. 2020, Nature Astronomy, 4, 609, doi: 10.1038/s41550-020-1009-3

Li, L., Baines, K. H., Smith, M. A., et al. 2012, Journal of Geophysical Research: Planets, 117, 1, doi: 10.1029/2012JE004191

Li, L., Jiang, X., West, R. A., et al. 2018, Nature Communications, 9, 3709, doi: 10.1038/s41467-018-06107-2

Lorenzen, W., Holst, B., & Redmer, R. 2009, Physical Review Letters, 102, doi: 10.1103/PhysRevLett.102.115701

—. 2011, Physical Review B, 84, doi: 10.1103/PhysRevB.84.235109

Lozovsky, M., Helled, R., Rosenberg, E. D., & Bodenheimer, P. 2017, The Astrophysical Journal, 836, doi: 10.3847/1538-4357/836/2/227

Mankovich, C., Fortney, J. J., & Moore, K. L. 2016, ApJ, 832, 13pp, doi: 10.3847/0004-637X/832/2/113

Mankovich, C. R., & Fortney, J. J. 2020, The Astrophysical Journal, 889, 51, doi: 10.3847/1538-4357/ab6210

Mankovich, C. R., & Fuller, J. 2021, Nature Astronomy, 5, 1103, doi: 10.1038/s41550-021-01448-3

Matson, D. L., Spilker, L. J., & Lebreton, J.-P. 2003, Space Science Reviews, 104, 1

Mazevet, S., Licari, A., Chabrier, G., & Potekhin, A. Y. 2019, A&A, 621, A128, doi: 10.1051/0004-6361/201833963

Militzer, B., & Hubbard, W. B. 2024, Icarus, 411, 115955, doi: 10.1016/j.icarus.2024.115955

Militzer, B., Wahl, S., & Hubbard, W. B. 2019, The Astrophysical Journal, 879, 78, doi: 10.3847/1538-4357/ab23f0

Militzer, B., Hubbard, W. B., Wahl, S., et al. 2022, The Planetary Science Journal, 3, 185, doi: 10.3847/PSJ/ac7ec8

Moll, R., Garaud, P., Mankovich, C., & Fortney, J. J. 2017, The Astrophysical Journal, 849, 24, doi: 10.3847/1538-4357/aa8d74

Moll, R., Garaud, P., & Stellmach, S. 2016, The Astrophysical Journal, 823, doi: 10.3847/0004-637X/823/1/33

Müller, S., & Helled, R. 2024, ApJ, 967, 7, doi: 10.3847/1538-4357/ad3738

Müller, S., Helled, R., & Cumming, A. 2020, A&A, 638, doi: 10.1051/0004-6361/201937376

Nettelmann, N. 2017, Astronomy and Astrophysics, 606, 1, doi: 10.1051/0004-6361/201731550

Nettelmann, N., Amoros, M. C., Tosi, N., Helled, R., & Fortney, J. J. 2024

Nettelmann, N., Fortney, J. J., Moore, K., & Mankovich, C. 2015, MNRAS, 447, 3422, doi: 10.1093/mnras/stu2634

Nettelmann, N., Movshovitz, N., Ni, D., et al. 2021, The Planetary Science Journal, 2, 18pp, doi: 10.3847/PSJ/ac390a

Paxton, B., Bildsten, L., Dotter, A., et al. 2011, The Astrophysical Journal Supplement Series, 192, 3, doi: 10.1088/0067-0049/192/1/3

Paxton, B., Cantiello, M., Arras, P., et al. 2013, The Astrophysical Journal Supplement Series, 208, 4, doi: 10.1088/0067-0049/208/1/4

Paxton, B., Schwab, J., Bauer, E. B., et al. 2018, ApJ, 234, 50pp, doi: 10.3847/1538-4365/aaa5a8

Petigura, E. A., Marcy, G. W., Winn, J. N., et al. 2018, The Astronomical Journal, 155, 89, doi: 10.3847/1538-3881/aaa54c

Püstow, R., Nettelmann, N., Lorenzen, W., & Redmer, R. 2016, Icarus, 267, 323, doi: 10.1016/j.icarus.2015.12.009

Rauer, H., Catala, C., Aerts, C., et al. 2014, Exp Astron, 38, 249, doi: 10.1007/s10686-014-9383-4

Rosenthal, L. J., Knutson, H. A., Chachan, Y., et al. 2021. https://arxiv.org/abs/2112.03399

Saumon, D., Chabrier, G., & Van Horn, H. M. 1995, The Astrophysical Journal Supplement Series, 99, 713

Schöttler, M., & Redmer, R. 2018, Physical Review Letters, 120, doi: 10.1103/PhysRevLett.120.115703

Seidelmann, P. K., Archinal, B. A., A'Hearn, M. F., et al. 2007, Celestial Mechanics and Dynamical Astronomy, 98, 155, doi: 10.1007/s10569-007-9072-y

Stacey, F. D., & Davis, P. M. 2004, Physics of the Earth and Planetary Interiors, 142, 137, doi: 10.1016/j.pepi.2004.02.003

Stevenson, D. J. 1975, Physical Review B, 12. https://journals.aps.org/prb/pdf/10.1103/PhysRevB.12.3999

—. 1982, Planetary and Space Science, 30, 755, doi: 10.1016/0032-0633(82)90108-8

Stevenson, D. J., Bodenheimer, P., Lissauer, J. J., & Angelo, G. D. . 2022, The Planetary Science Journal, 3, 15pp, doi: 10.3847/PSJ/ac5c44

Stevenson, D. J., & Salpeter, E. E. 1977, The Astrophysical Journal Supplement Series, 35, 221. https://articles.adsabs.harvard.edu/pdf/1977ApJS...35..221S

Sur, A., Su, Y., Arevalo, R. T., Chen, Y.-X., & Burrows, A. 2024, The Astrophysical Journal, 971, 104, doi: 10.3847/1538-4357/ad57c3

Tejada Arevalo, R., Su, Y., Sur, A., & Burrows, A. 2024, The Astrophysical Journal Supplement Series, 274, 34, doi: 10.3847/1538-4365/ad6cd7

Tinetti, G., Eccleston, P., Haswell, C., et al. 2021, arXiv e-prints, arXiv:2104.04824, doi: 10.48550/arXiv.2104.04824

Tulekeyev, A., Garaud, P., Idini, B., & Fortney, J. J. 2024, PSJ, 5, 190, doi: 10.3847/PSJ/ad6571

Vazan, A., Helled, R., & Guillot, T. 2018, A&A, 610, 14, doi: 10.1051/0004-6361/201732522

Vazan, A., Helled, R., Podolak, M., & Kovetz, A. 2016, ApJ, 829, doi: 10.3847/0004-637X/829/2/118

Von Zahn, U., Hunten, D. M., & Lehmacher, G. 1998, Journal of Geophysical Research: Planets, 103, 22815, doi: 10.1029/98JE00695

Wahl, S. M., Hubbard, W. B., Militzer, B., et al. 2017, Geophysical Research Letters, 44, 4649, doi: 10.1002/2017GL073160

Wilson, H. F., & Militzer, B. 2010, Physical Review Letters, 104, 1, doi: 10.1103/PhysRevLett.104.121101

Winn, J. N., & Fabrycky, D. C. 2015, Annual Review of Astronomy and Astrophysics, 53, 409, doi: 10.1146/annurev-astro-082214-122246

Wood, T. S., Garaud, P., & Stellmach, S. 2013, The Astrophysical Journal, 768, 157, doi: 10.1088/0004-637X/768/2/157

Yu, Z. J., & Russell, C. T. 2009, Geophysical Research Letters, 36, 26, doi: 10.1029/2009GL040094

Zhang, J., & Rogers, L. A. 2022, The Astrophysical Journal, 938, 131, doi: 10.3847/1538-4357/ac8e65